

Electronic supplementary information

Boosting reaction kinetics of polycrystalline phase Fe₇S₈/FeS₂ heterostructures encapsulated in hollow carbon nanofiber for superior fast sodium storage

Hui Cai^{‡a,b}, Fei Wang^{‡b,c}, Huiyan Feng^{‡a,b}, Zhendong Liu^{a,b}, Chengzhi Zhang^{b*}, Anbang Lu^{a,b}, Xia Zhao^b, Qihong Lu^{b*}, Quanbing Liu^{b*}, and Jun Tan^{b,d*}

^aSchool of Chemical Engineering and Light Industry, Guangdong University of Technology, Guangzhou, Guangdong, 510006, China

^bJi Hua Laboratory, Foshan, Guangdong, 528000, China

^cHunan Province Key Laboratory for Advanced Carbon Materials and Applied Technology, College of Materials Science and Engineering, Hunan University, Changsha, 410082, China

^dFoshan University, Foshan, Guangdong, 528000, China

‡ The authors contributed equally to this work.

*Corresponding authors

Chengzhi Zhang, Ji Hua Laboratory, Foshan, Guangdong, 528000, China.

Email: zhangchz@jihualab.ac.cn

Qihong Lu, Ji Hua Laboratory, Foshan, Guangdong, 528000, China.

Email: luqh@jihualab.ac.cn

Jun Tan, Ji Hua Laboratory, Foshan, Guangdong, 528000, China.

Email: tanjun@jihualab.ac.cn

Quanbing Liu, Guangdong University of Technology, Guangzhou, Guangdong, 510006, China

Email: liuqb@gdut.edu.cn

Experimental

Synthesis of Materials

Preparation of NHCFs-Fe₂O₃ precursor: In a typical preparation process, 0.78 g methyl orange was dissolved in 500 mL deionized water, then 3.89 g ferric chloride was added until the mixture was uniform, and 0.94 mL pyrrole monomer was added and stirred for 24 h. Finally, the black solution was centrifuged and washed to obtain hollow polypyrrole (PPy) nanotubes, which were dried in vacuum at 80 °C for use. Then, 0.5 mol L⁻¹ Fe(NO₃)₃ solution (30 mL) and 0.7 mol L⁻¹ Na₂CO₃ solution (30 mL) were slowly added to the deionized water (60 mL) of dispersed hollow PPy nanotubes (0.3 g) by a constant flow pump, and slowly stirred during the drip process. After the drip is completed, continue to stir for 2 h, centrifugal collection, and then vacuum drying at 80°C for 24 h to obtain PPy-Fe₂O₃. Finally, the NHCFs-Fe₂O₃ precursor was obtained by annealing it in an argon atmosphere at 550 °C for 4 h.

Preparation of NHCFs-Fe₇S₈ and NHCFs-FeS₂ composites: For the preparation of NHCFs-Fe₇S₈ composites, the obtained NHCFs-Fe₂O₃ was placed in an alumina boat and heated to 550 °C under the atmosphere of argon and CS₂ in a tube furnace for 2 h, and the heating rate was 5 °C min⁻¹ for sulphuration process to obtain NHCFs-Fe₇S₈. For the preparation of NHCFs-FeS₂ composites, NHCFs-Fe₂O₃ and sulfur powder (mass ratio 1:10) were fully ground and placed on an alumina boat. In an argon atmosphere, the furnace was heated to 550 °C for 2 h and the heating rate was 5 °C min⁻¹ for sulphuration process to obtain NHCFs-FeS₂.

Preparation of NHCFs-Fe₇S₈/FeS₂ polycrystalline phase: Briefly, NHCFs-Fe₇S₈ above and sulfur powder (mass ratio 1:20) are fully ground, placed on an alumina boat, and then put in the center of the tube furnace. The NHCFs-Fe₇S₈/FeS₂ polycrystalline phase was obtained by heating up to 550 °C for 2 h at 5 °C min⁻¹ in an argon atmosphere.

Material characterization

The structure and morphology of samples were observed by field-emission scanning electron microscope (FESEM, Thermo Fisher Scientific Verios 5 UC) and high-resolution transmission electron microscope (HRTEM, Thermo Fisher Scientific Talos F200X). The crystal structure of the composites was studied by X-ray diffraction (XRD, Bruker D8 DISCOVER, Cu-K_α). The chemical composition of samples was revealed by raman spectrometer (Renishaw inVia, 532 nm). The elemental composition of the composites was obtained by X-ray photoelectron spectroscopy (XPS, Thermo Fisher Scientific Escalab Xi⁺).

The carbon content of sample has been studied by the thermogravimetric analysis (TGA, TA TGA 5500).

Electrochemical measurements

The working electrodes were fabricated through a process of coating a mixture of active samples, sodium alginate, and conductive carbon black in an 8:1:1 ratio using water as a solvent onto copper foil. The resulting slurry was uniformly applied and the electrodes were then vacuum dried at 80°C overnight before being cut into 12 mm diameter discs with a mass loading of approximately 2.0 mg cm⁻². An electrolyte of 1.0 M NaPF₆ in diglyme (DME) was utilized in the assembly of a CR2025 type button cell within a glove box. Constant current discharge/charge tests were conducted using a LAND battery test system across a wide voltage window of 0.005-3.0 V. Additionally, cyclic voltammetry (CV) curves and electrochemical impedance spectroscopy (EIS) measurements were performed on a Bio-Logic electrochemistry workstation at frequencies ranging from 100 kHz to 10 mHz, over a voltage range of 0.005-3.0 V at various scan rates.

For the preparation of full cell, the as-prepared anode was pre-sodiated via contacting with Na metal for 1 hours. The Na₃V₂(PO₄)₃/C on Al foil was employed as the cathode (the electrode diameter is 13 mm), and the n/p ratio of all full-cell defined as the anode areal capacity over cathode areal capacity was set to 1.1. The fabrication process for assembling full cell is same with that for preparing the half cell, which is a button cell. The full cell tests (1C = 110 mA g Na₃V₂(PO₄)₃⁻¹) were conducted in the potential range of 1.0 - 3.5 V. The full cell at 0.11 A g⁻¹ were processed under constant current (CC) mode for charging and discharging.

Computational methods

In this work, the simulation is based on density functional theory (DFT) and the Perdew-Burke-Ernzerhof function of generalized gradient approximation. Specifically, the DFT-D3 method was adopted, and the stable crystal structure information of the system was used to analyze the bonding of the polycrystalline phase system by using the electronic iteration algorithm and geometric optimization methods. The cut-off energy used in the expansion of the plane wave is 450 eV, and the self-consistent field energy convergence threshold is set to 10⁻⁶ eV. Differential charge density is used to analyze the trend of charge movement in the interface. The diffusion barrier of sodium ions in each structure was analyzed by CI-NEB method. Using the VASP algorithm, the force is calculated with an accuracy of 1E-7. All calculations are performed on the basis of structural relaxation.

Supplementary Figures

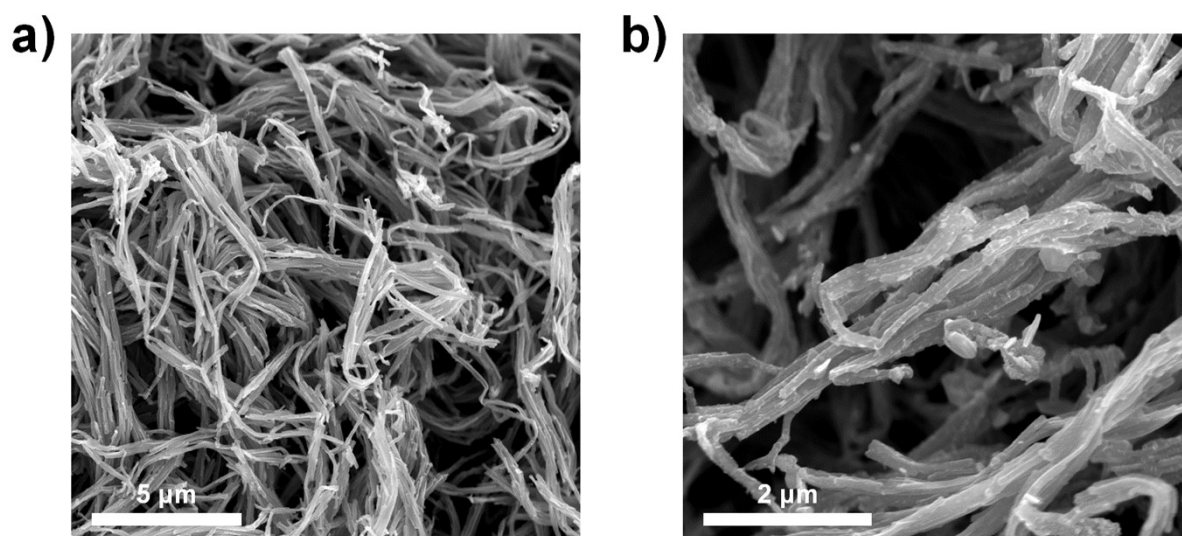


Fig. S1. SEM image of a) PPy and b) NHCFS-Fe₂O₃.

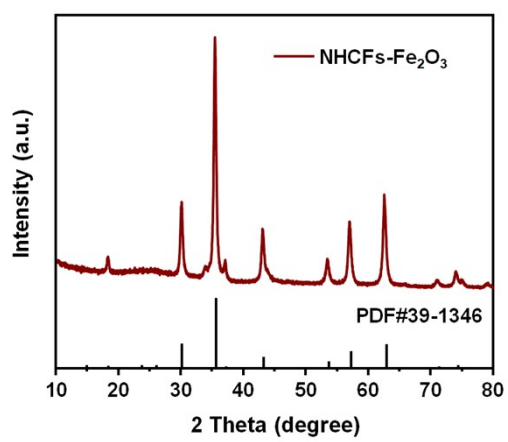


Fig. S2. XRD pattern of NHCFS-Fe₂O₃.

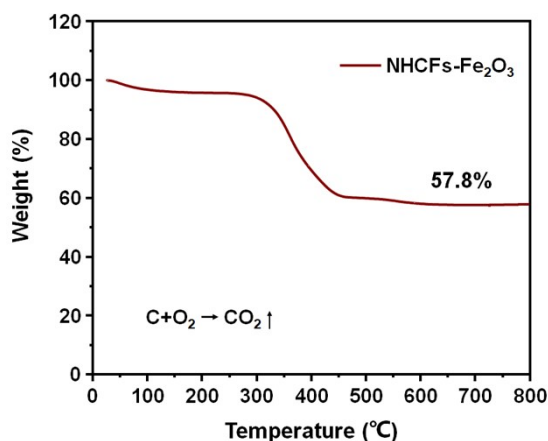


Fig. S3. The thermogravimetric curves of NHCFS-Fe₂O₃.

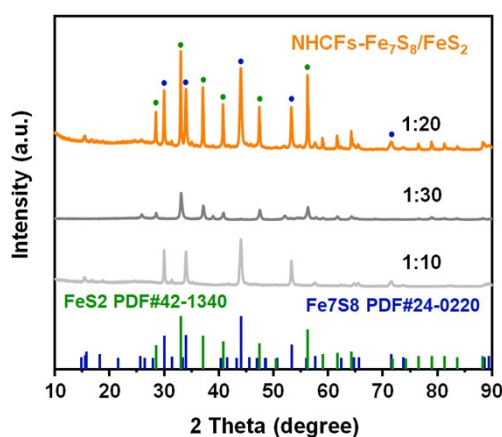


Fig. S4. XRD patterns of the composites of polycrystalline heterostructures of Fe₇S₈ and FeS₂ with different proportions.

Based on the Fe-S phase diagram, the formation temperature of Fe₇S₈ phase is at least 800 K (about 550 °C). The higher treatment temperature could cause lower C-S doped in carbon skeleton, which reduces the stability of the product. To obtain a stable Fe₇S₈ phase, we adjusted the ratio of S powder to the target product, but pure phase Fe₇S₈ could not be obtained only by adjusting the ratio. Thus, we changed the S sources to CS₂. Firstly, CS₂ contains C atom which is benefited to the formation of C-S bonds, secondly, the CS₂ could successful composite the Fe₇S₈ phase.

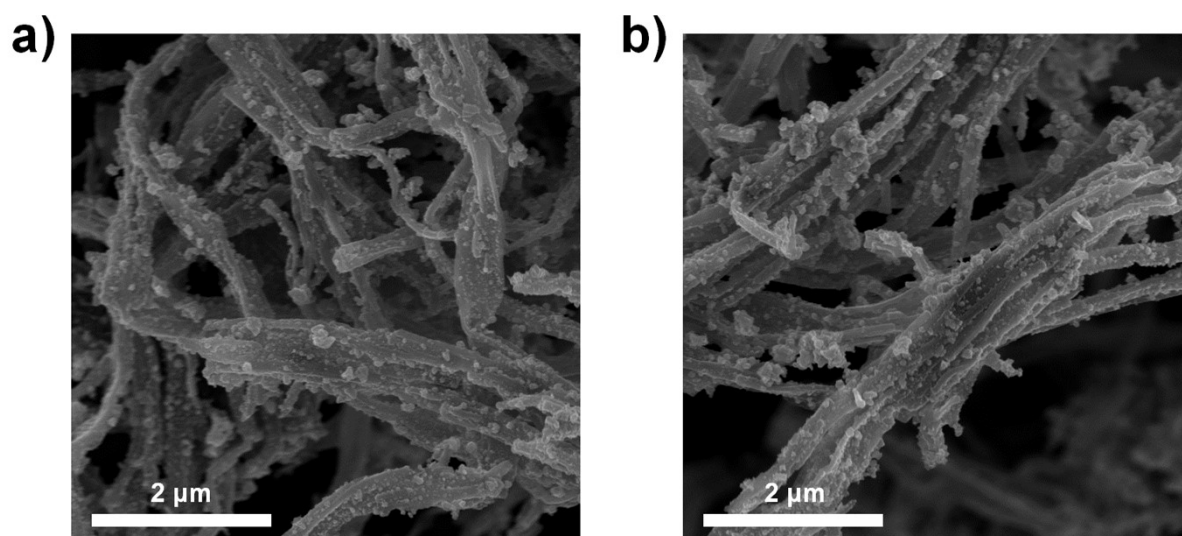


Fig. S5. SEM image of a) NHCs-Fe₇S₈ and b) NHCs-FeS₂.

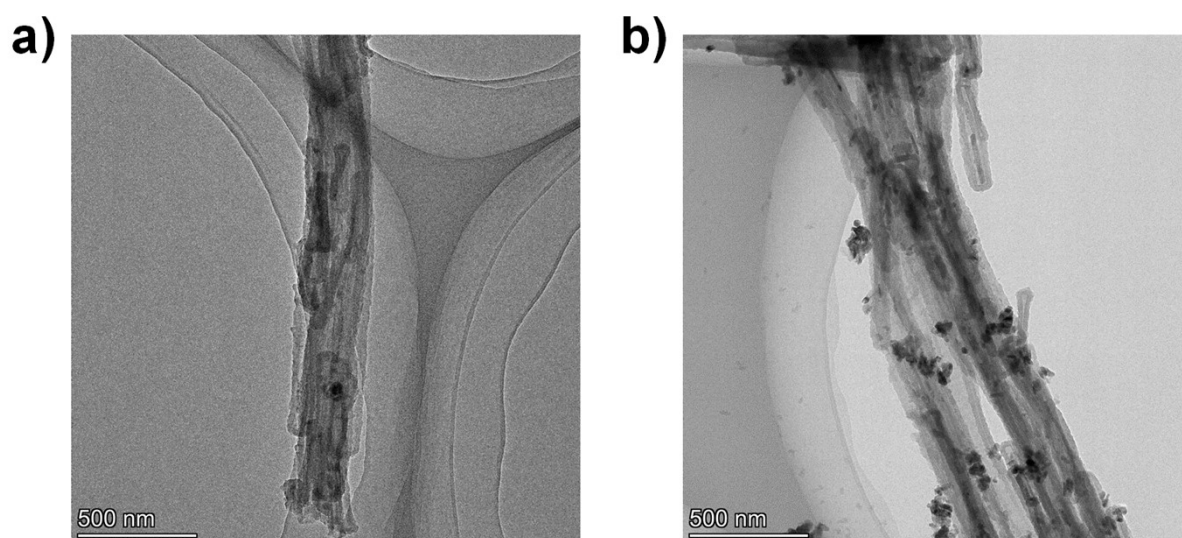


Fig. S6. TEM image of a) NHCs-Fe₇S₈ and b) NHCs-FeS₂.

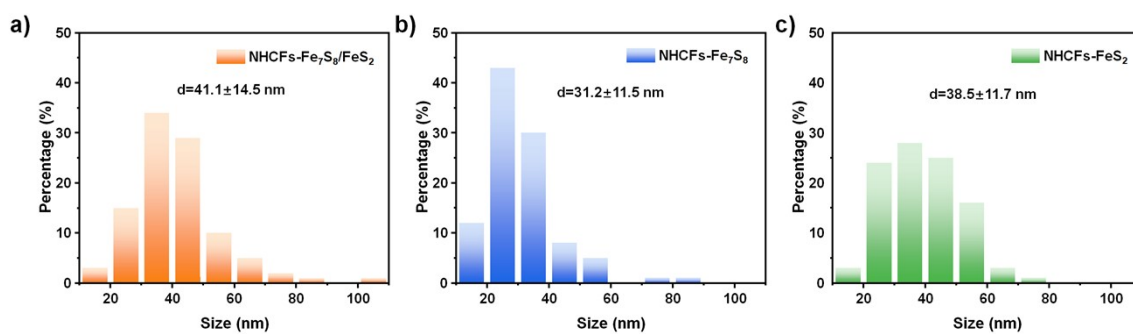


Fig. S7. Size distributions of a) NHCfS-Fe₇S₈/FeS₂, b) NHCfS-Fe₇S₈ and c) NHCfS-FeS₂.

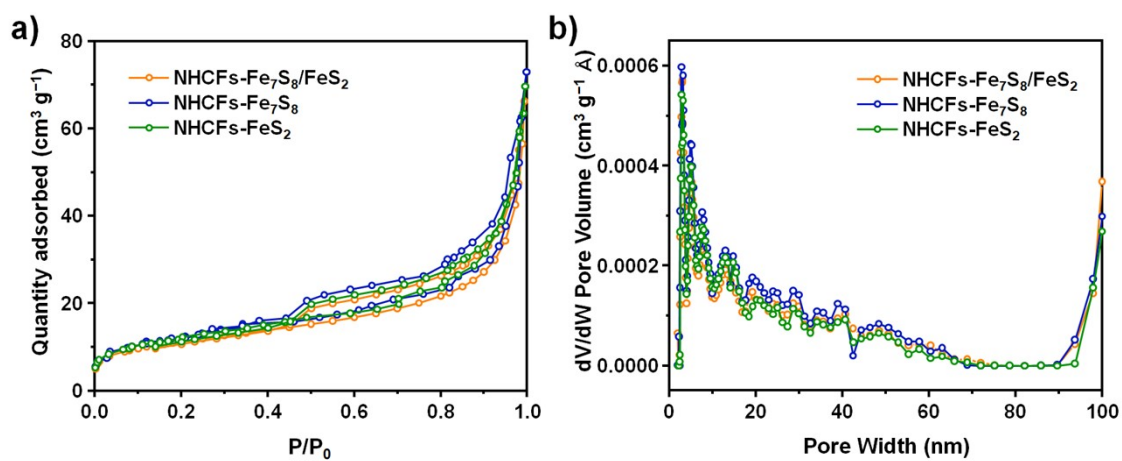


Fig. S8. a) Nitrogen adsorption–desorption isotherms and b) pore size distributions of NHCfS-Fe₇S₈/FeS₂, NHCfS-Fe₇S₈ and NHCfS-FeS₂.

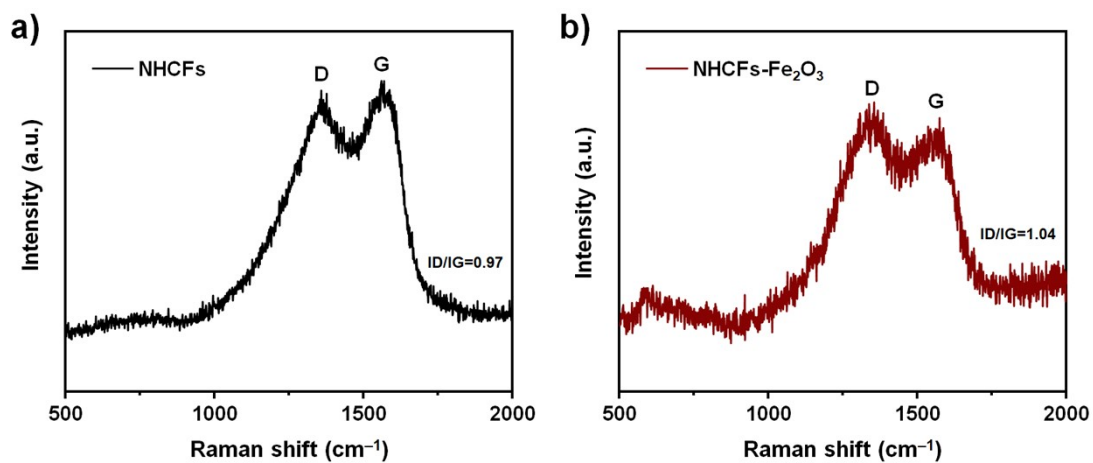


Fig. S9. Raman spectrum of a) PPy and b) NHCFS-Fe₂O₃.

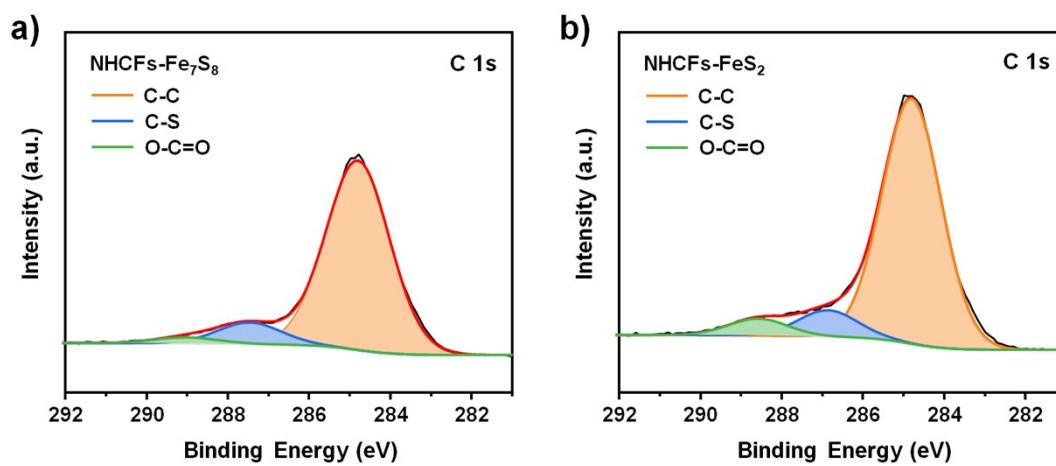


Fig. S10. The high-resolution XPS spectra C 1s of a) NHCFS-Fe₇S₈ and b) NHCFS-FeS₂.

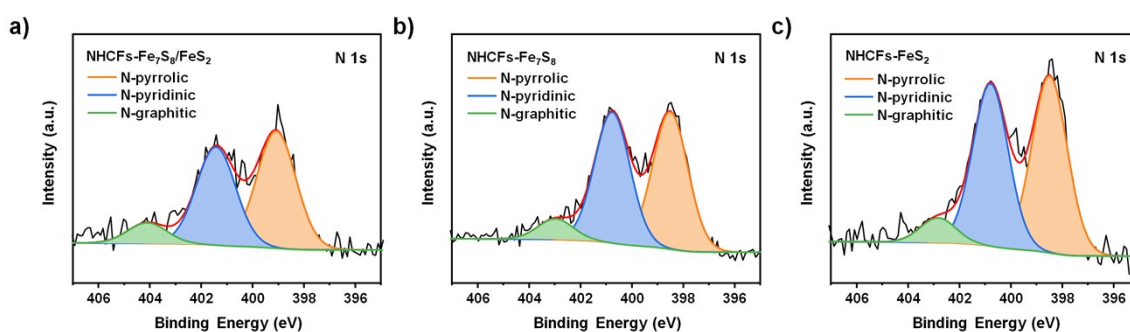


Fig. S11. The high-resolution XPS spectra N 1s of a) NHCfS-Fe₇S₈/FeS₂, b) NHCfS-Fe₇S₈ and c) NHCfS-FeS₂.

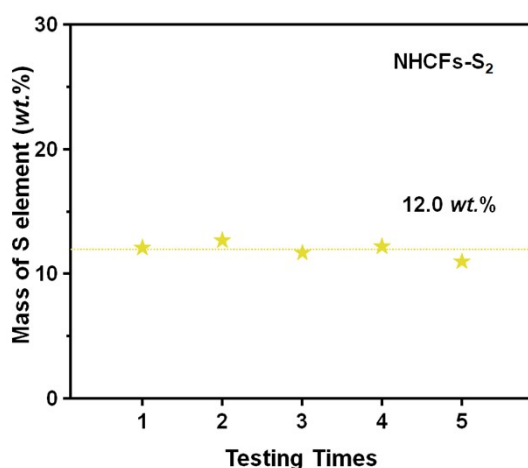


Fig. S12. The mass ratio of S element in the carbon tube after a two-step sulphuration method which tested by Elemental Analysis. (NHCfS-S₂).

In the thermogravimetric curve of polycrystalline NHCfS-Fe₇S₈/FeS₂ composites, the first weight loss before 300 °C is mainly due to the loss of absorbed water and the combustion of sulfur atom in the carbon skeleton. Later, the apparent weight loss was attributed to the combustion of the carbon skeleton and the subsequent oxidation of the Fe₇S₈/FeS₂ nanoparticles.

We assume the weight percentage of Fe₇S₈ is x , and the weight percentage of FeS₂ is y , then the percentage of the final product Fe₂O₃ is as follows:

$$\text{Fe}_2\text{O}_3(\text{wt.}\%) = \left(\frac{14 \times \text{molecular weight of Fe}_2\text{O}_3 \times \text{weight of Fe}_7\text{S}_8}{4 \times \text{molecular weight of Fe}_7\text{S}_8} + \frac{2 \times \text{molecular weight of Fe}_2\text{O}_3 \times \text{weight of FeS}_2}{4 \times \text{molecular weight of FeS}_2} \right) \times 100\% = \left(\frac{14 \times 159.7 \times x}{4 \times 647.4} + \frac{2 \times 159.7 \times y}{4 \times 120} \right) \times 100\% = 41.3 \text{ wt.}\%$$

As shown in Fig. S12, on the carbon skeleton without in-situ growth of iron particles, elemental analysis was performed after sulphuration steps under the same conditions as that of synthetic NHCFs-Fe₇S₈/FeS₂, the mass ratio of S element in carbon skeleton was about 12.0 wt.%. According to the 41.3 wt.% Fe₂O₃ remaining after the complete reaction of NHCFs-Fe₇S₈/FeS₂, the content of Fe element in the composites is calculated to be 28.9 wt.%. Since the mass ratio of Fe element to pure carbon skeleton is not changed during the sulphuration process, the mass ratio of pure carbon skeleton of polycrystalline phase NHCFs-Fe₇S₈/FeS₂ composites is 30.2 wt.%.

$$\text{NHCFs}(\text{wt.}\%) = \frac{\text{weight of Fe element of NHCFs - Fe}_7\text{S}_8/\text{FeS}_2 \times \text{weight of pure carbon skeleton of NHCFs - Fe}_2\text{O}_3}{\text{weight of Fe element of NHCFs - Fe}_2\text{O}_3} \times 100\% = \frac{28.9 \times 42.2}{40.4} \times 100\% = 30.2 \text{ wt.}\%$$

Thus, the mass ratio of Fe₇S₈/FeS₂ in the NHCFs-Fe₇S₈/FeS₂ is 57.8 wt.%.

$$x + y = 57.8 \text{ wt.}\% \quad x = 13.4 \text{ wt.}\%, y = 44.5 \text{ wt.}\%$$

Thus, the mass ratio of Fe₇S₈ is 13.4 wt.%, and the mass ratio of FeS₂ is 44.5 wt.%. The molar ratio between Fe₇S₈ and FeS₂ in the NHCFs-Fe₇S₈/FeS₂ is about 1:18.

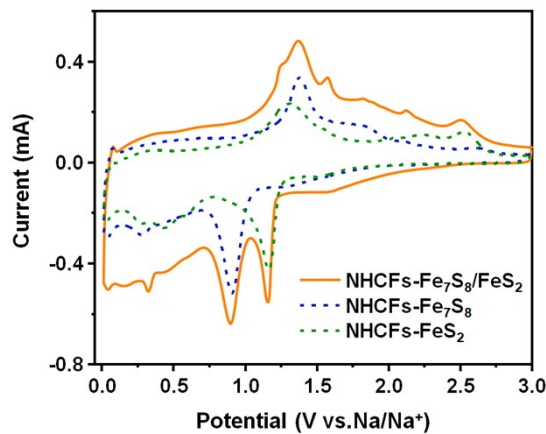


Fig. S13. Comparison of the first CV curves at 0.2 mV s^{-1} of NHCFs- $\text{Fe}_7\text{S}_8/\text{FeS}_2$, NHCFs- Fe_7S_8 and NHCFs- FeS_2 .

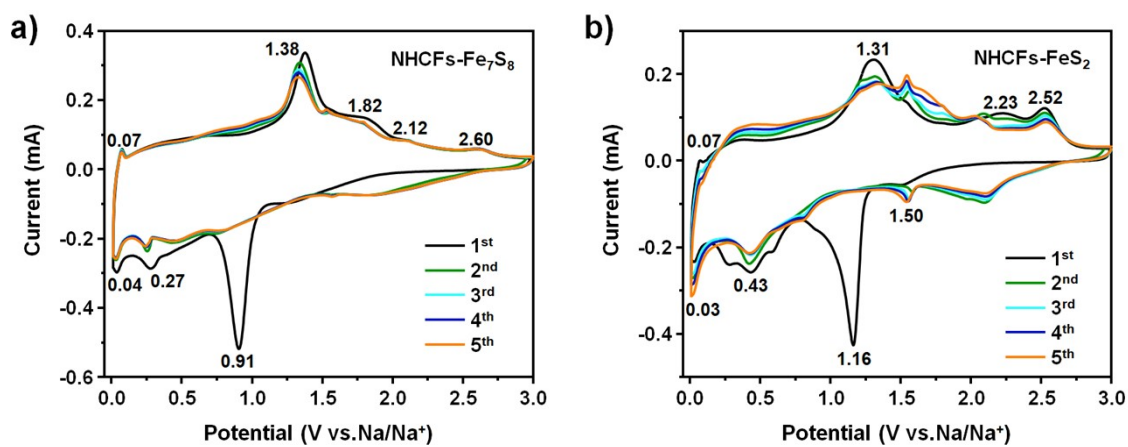


Fig. S14. The CV curves of a) NHCfS-Fe₇S₈ and b) NHCfS-FeS₂ at a scan rate of 0.2 mV s⁻¹.

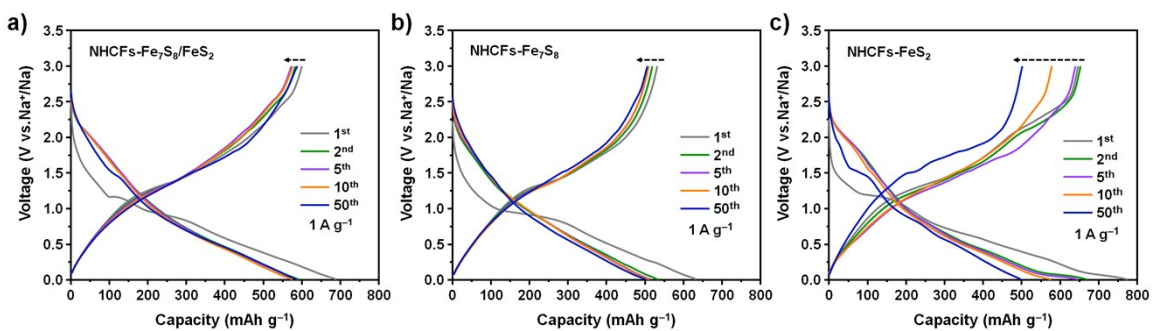


Fig. S15. The corresponding galvanostatic discharge/charge profiles of a) NHCfS-Fe₇S₈/FeS₂, b) NHCfS-Fe₇S₈ and c) NHCfS-FeS₂.

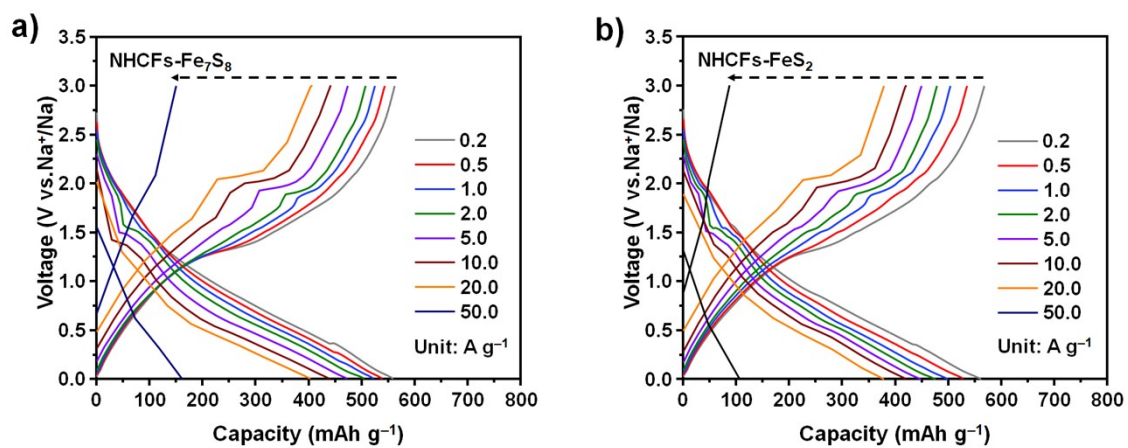


Fig. S16. The capacity-voltage curves increasing from 0.2 to 50 A g⁻¹ of a) NHCfS-Fe₇S₈ and b) NHCfS-FeS₂.

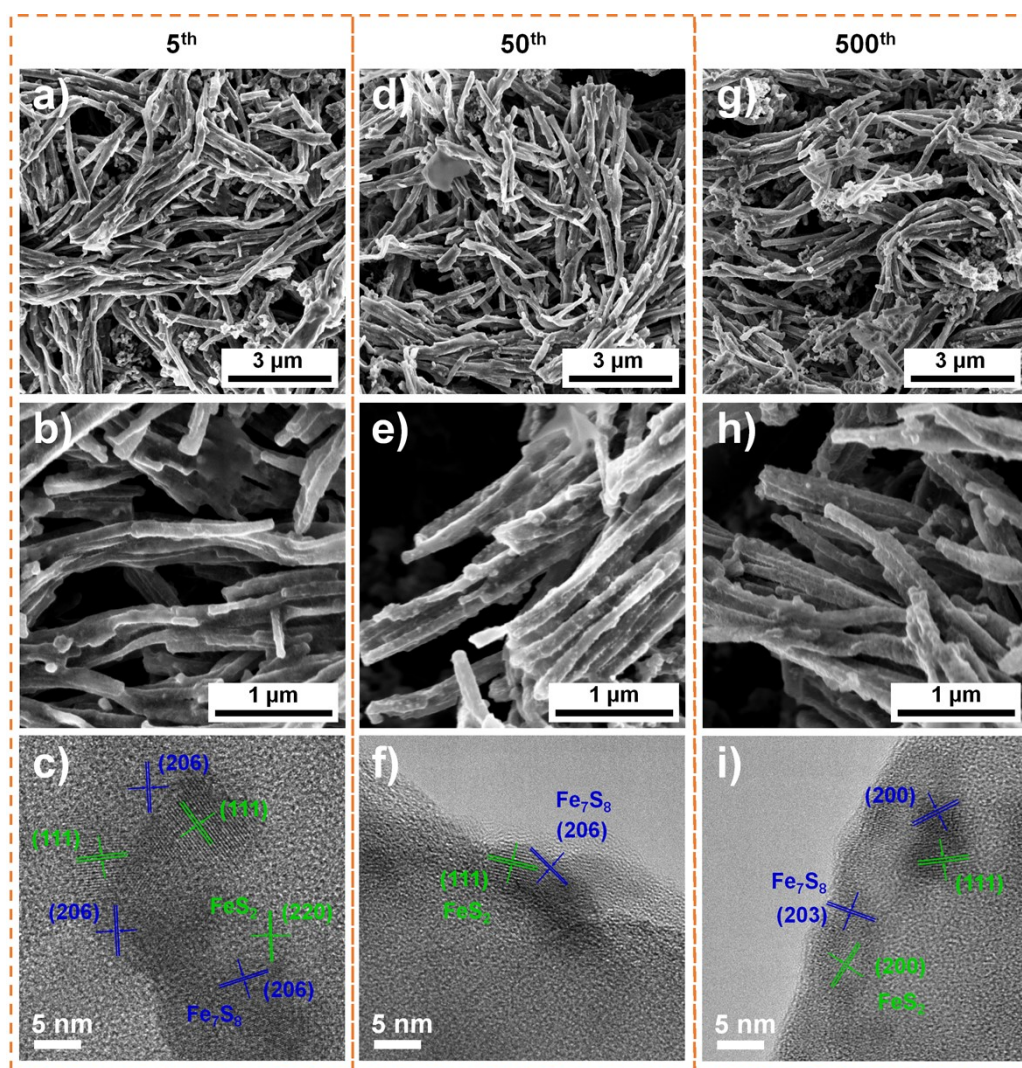


Fig. S17. SEM images and HRTEM images of NHCfS-Fe₇S₈/FeS₂ electrode anode for the (a, b, c) 5, (d, e, f) 50 and (g, h, i) 500 cycles of sodium storage.

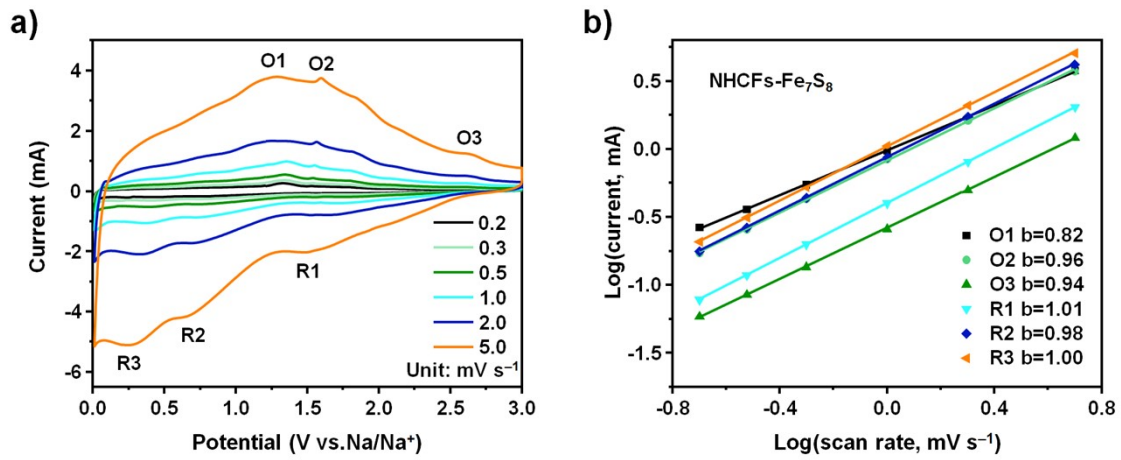


Fig. S18. a) CV curves of NHCFS- Fe_7S_8 electrode at different scan rates. b) The plots of peak current versus scan rate for NHCFS- Fe_7S_8 electrode.

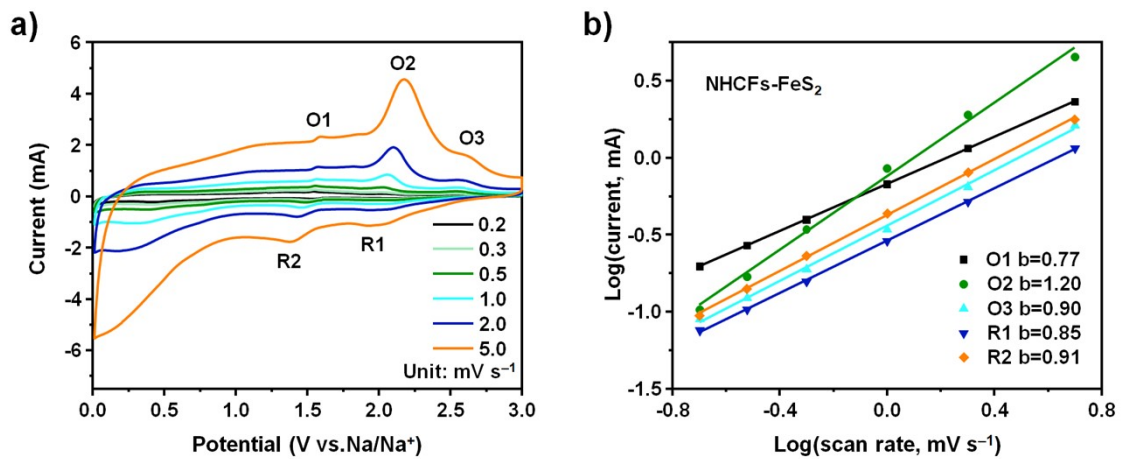


Fig. S19. a) CV curves of NHCFS- FeS_2 electrode at different scan rates. b) The plots of peak current versus scan rate for NHCFS- FeS_2 electrode.

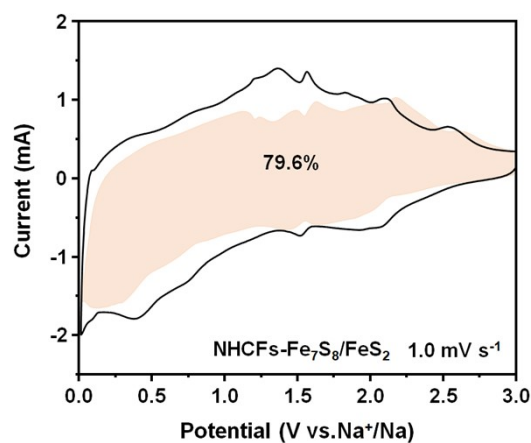


Fig. S20. The diffusion and capacitive contributions of sodium storage for NHCFS-Fe₇S₈/FeS₂ at the scan rate of 1.0 mV s⁻¹.

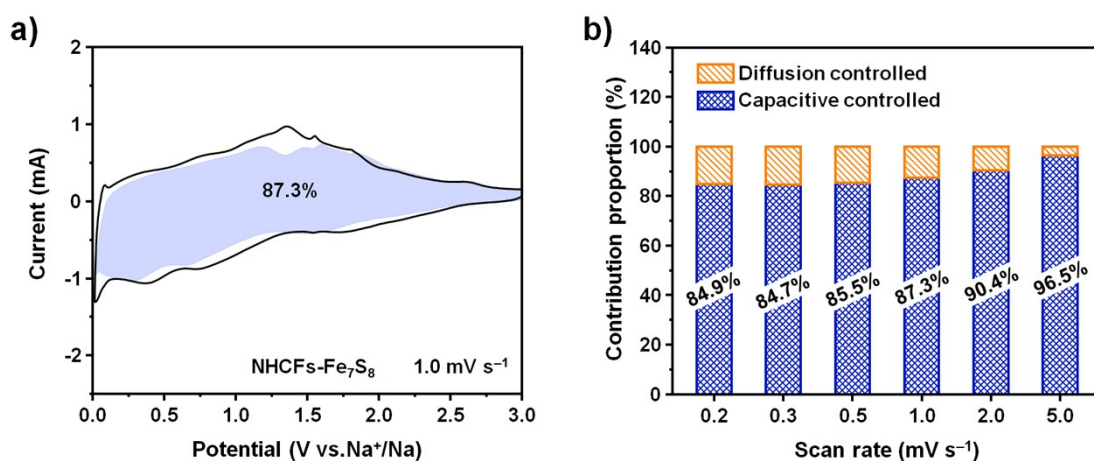


Fig. S21. a) The diffusion and capacitive contributions of sodium storage for NHCFS-Fe₇S₈ at the scan rate of 1.0 mV s⁻¹, and b) The percentage for capacitance contribution of NHCFS-Fe₇S₈ at different scan rates.

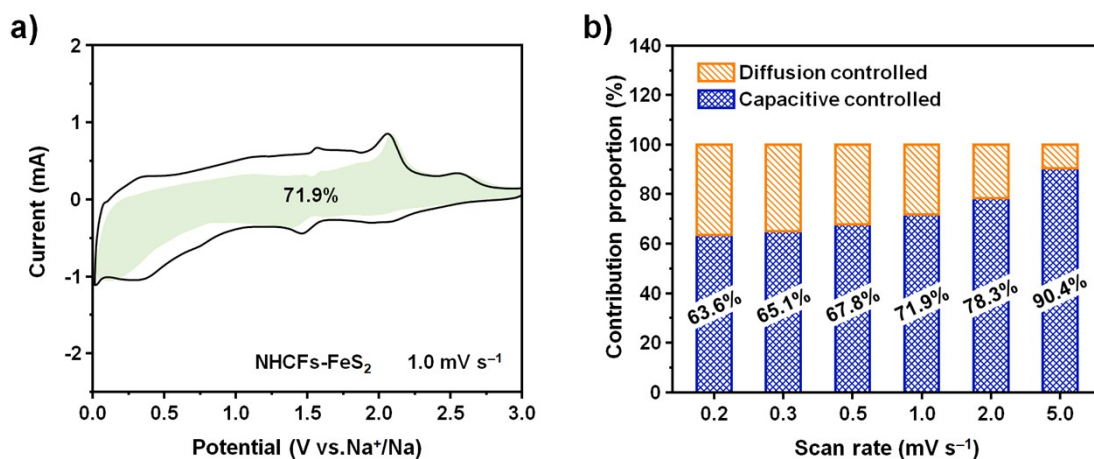


Fig. S22. a) The diffusion and capacitive contributions of sodium storage for NHCFS-FeS₂ at the scan rate of 1.0 mV s⁻¹, and b) The percentage for capacitance contribution of NHCFS-FeS₂ at different scan rates.

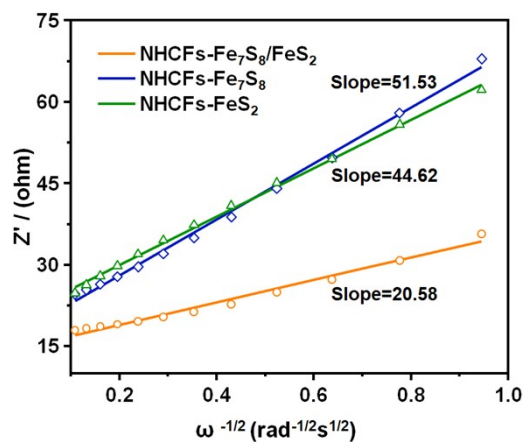


Fig. S23. The plots of ω^{1/2} versus Z' curves in the low-frequency area of NHCFS-Fe₇S₈/FeS₂, NHCFS-Fe₇S₈ and NHCFS-FeS₂ before cycling.

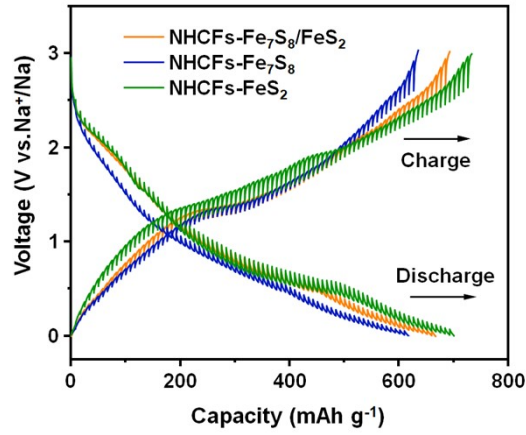


Fig. S24. The GITT curves of NHCFS-Fe₇S₈/FeS₂, NHCFS-Fe₇S₈ and NHCFS-FeS₂.

The sodium-ion diffusion coefficient D_{Na^+} ($\text{cm}^2 \text{s}^{-1}$) was determined through Galvanostatic Intermittent Titration Technique (GITT) results. The value of D_{Na^+} was calculated using the

Fick's second law:
$$D = \frac{4}{\pi\tau} \left(\frac{m_B V_M}{M_B S} \right)^2 \left(\frac{\Delta E_s}{\Delta E_t} \right)^2$$
. In the Equation, M_B represents the molar mass of active material, S means the electrode area, V_M equals to the molar volume of the active materials, m_B describes the mass of active material, and τ denotes the current time.

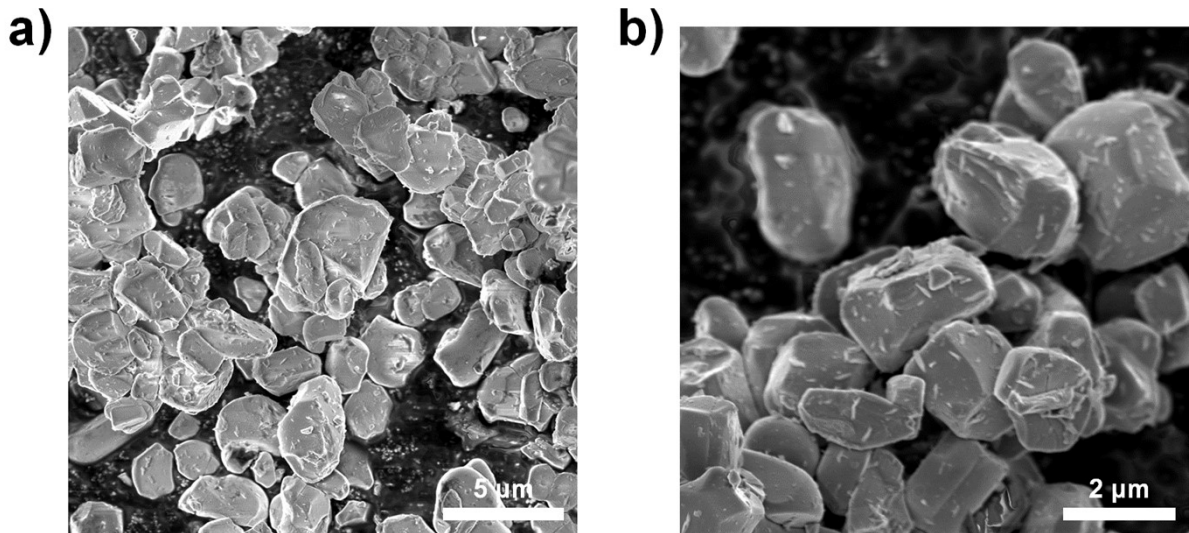


Fig. S25. SEM image of Na₃V₂(PO₄)₃ (NVP).

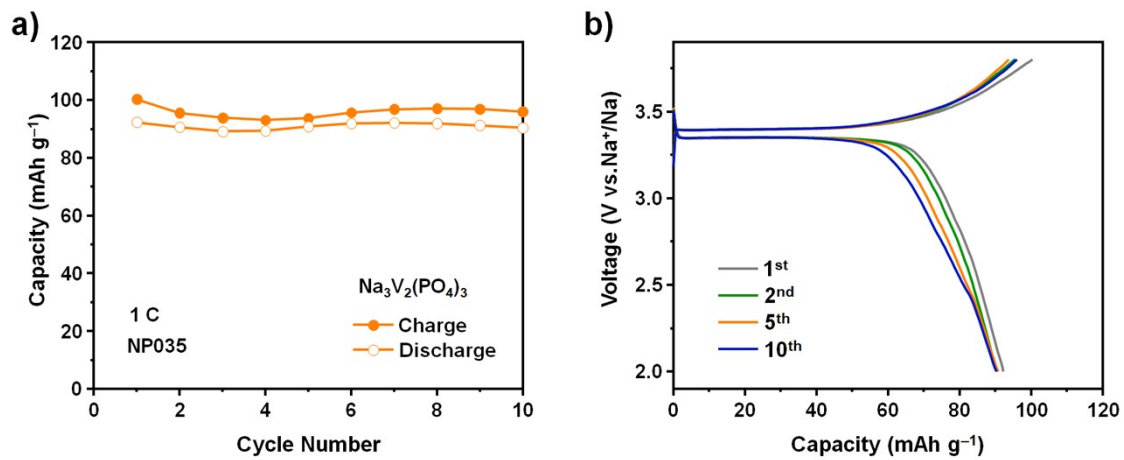


Fig. S26. a) The cycling performance and b) the corresponding galvanostatic discharge/charge profiles of NVP at the current density of 1.0 C.

Table S1. Comparison of electrochemical data of NHCFs-Fe₇S₈/FeS₂ in this work with recently reported transition metal sulfide-based heterojunction anode materials for sodium ion batteries.

Sample	Cut-off voltage (V)	Cycling stability			Rate capability		Ref.	
		ICE (%)	Current density (A g ⁻¹)	Cycle number	Capacity retention (mAh g ⁻¹)	Current density (A g ⁻¹)		Capacity retention (mAh g ⁻¹)
NHCFs-Fe₇S₈/FeS₂	0.005-3.0	85.3	1	1000	596	50/100	269/107	This work
ZnS/Fe ₉ S ₁₀ @C	0.005-3.0	85.3	1	200	485	50	235	1
SnS/MoS ₂ /NS-CNs	0.01-3.0	69.8	1	800	287.2	5	372.9	2
(SnCo)S ₂ /SG	0.01-3.0	78.6	5	5000	487	10	469	3
L-Sb ₂ S ₃ /Ti ₃ C ₂	0.005-3.0	65.7	1	100	358.2	2	339.5	4
SnS/Fe _{1-x} S@SC	0.01-3.0	74.3	2	2900	310	1	491	5
ZnS/Sb ₂ S ₃ @NC	0.01-3.0	68.0	2	450	511.4	10	400.4	6
Bi ₂ S ₃ -CuS/C	0.01-3.0	97.2	8	1000	592.2	20	459.9	7
Sb ₂ S ₃ /MoS ₂ @C	0.1-3.0	75.9	5	650	411.5	10	408.7	8
Fe ₉ S ₁₀ @MoS ₂ @C	0.005-3.0	80.1	2	1000	355	30/50	197/132	9
MoO ₂ /MoS ₂ /C	0-3.0	/	1	1000	324	5	273	10
Fe ₇ S ₈ /FeS ₂ /NCNT	0.01-3.0	73.4	5	1000	466.7	20	536.5	11

References

- 1 C. Zhang, F. Han, J. Ma, Z. Li, F. Zhang, S. Xu, H. Liu, X. Li, J. Liu and A.-H. Lu, Fabrication of strong internal electric field ZnS/Fe₉S₁₀ heterostructures for highly efficient sodium ion storage, *J. Mater. Chem. A*, 2019, **7**, 11771-11781.
- 2 D. Wang, L. Cao, D. Luo, R. Gao, H. Li, D. Wang, G. Sun, Z. Zhao, N. Li, Y. Zhang, F. Du, M. Feng and Z. Chen, Chain mail heterostructured hydrangea-like binary metal sulfides for high efficiency sodium ion battery, *Nano Energy*, 2021, **87**, 106185.
- 3 C. Yang, X. Liang, X. Ou, Q. Zhang, H.-S. Zheng, F. Zheng, J.-H. Wang, K. Huang and M. Liu, Heterostructured nanocube-shaped binary sulfide (SnCo)S₂ interlaced with S-doped graphene as a high-performance anode for advanced Na⁺ batteries, *Adv. Funct. Mater.*, 2019, **29**, 1807971.
- 4 F. He, C. Tang, G. Zhu, Y. Liu, A. Du, Q. Zhang, M. Wu and H. Zhang, Leaf-inspired design of mesoporous Sb₂S₃/N-doped Ti₃C₂T_x composite towards fast sodium storage, *Sci China Chem*, 2021, **64**, 964-973.
- 5 F. Zhao, X. Xiao, L. Yang, Z. Wang, S. Xu and J. Liu, Synergistical coupling Janus SnS-Fe_{1-x}S heterostructure cell and polydopamine-derived S doped carbon as high-rate anodes for sodium-ion batteries, *Chem. Eng. J.*, 2021, **425**, 130534.
- 6 C. Dong, H. Shao, Y. Zhou, W. Du, L. Li, J. Sun, Z. Yan, Z. Hu, S. Chou and F. Jiang, Construction of ZnS/Sb₂S₃ heterojunction as an ion-transport booster toward high-performance sodium storage, *Adv. Funct. Mater.*, 2023, **33**, 2211864.
- 7 Z. Zhao, K. Li, C. Li, X. Pei, S. Zhang, Z. Liu, X. Du and D. Li, Defective Bi₂S₃ anchored on CuS/C as an ultrafast and long-life anode for sodium-ion storage, *ACS Appl. Mater. Interfaces*, 2023, **15**, 4011-4020.
- 8 L. Cui, C. Tan, G. Yang, Y. Li, Q. Pan, M. Zhang, Z. Chen, F. Zheng, H. Wang and Q. Li, Constructing an interface synergistic effect from a SnS/MoS₂ heterojunction decorating N, S co-doped carbon nanosheets with enhanced sodium ion storage performance, *J. Mater. Chem. A*, 2020, **8**, 22593-22600.
- 9 C. Zhang, F. Han, F. Wang, Q. Liu, D. Zhou, F. Zhang, S. Xu, C. Fan, X. Li and J. Liu, Improving compactness and reaction kinetics of MoS₂@C anodes by introducing Fe₉S₁₀ core for superior volumetric sodium/potassium storage, *Energy Stor. Mater.*, 2020, **24**, 208-219.
- 10 X. Li, R. Wang, Q. Wu, Y. Yu, T. Gao, T. Yao, X. Wang, J. Han and B. Song, Synergistically designed dual interfaces to enhance the electrochemical performance of MoO₂/MoS₂ in Na- and Li-ion batteries, *Small*, 2023, **19**, 2206940.
- 11 P. Song, J. Yang, C. Wang, T. Wang, H. Gao, G. Wang and J. Li, Interface engineering of Fe₇S₈/FeS₂ heterostructure in situ encapsulated into nitrogen-doped carbon nanotubes for high power sodium-ion batteries, *Nano-Micro Lett.*, 2023, **15**, 118.